Materials Today Communications 47 (2025) 112924

Contents lists available at ScienceDirect

Materials Today Communications

journal homepage: www.elsevier.com/locate/mtcomm

Realistic microstructural modeling of supercrystalline oleic acid nanocomposites

V. Kolli [a,c,*], I. Scheider [a], K. Schneider [b], D. Giuntini [d], C. Cyron [a,c]

[a] Helmholtz Zentrum Hereon, Institute for Material Systems Modeling, Max–Planck-Straße 1, Geesthacht, 21502, Schleswig - Holstein, Germany
[b] Hamburg University of Technology, Institute of Structural Mechanics in Lightweight Design, Eißendorfer Straße 40, Hamburg, 21073, Germany
[c] Hamburg University of Technology, Institute for Continuum and Material Mechanics, Eißendorfer Str. 42 (Geb. M), Hamburg, 21073, Germany
[d] Eidhoven University of Technology, Department of Mechanical Engineering, De Rondom 70, Eidnhoven, 5612 AP, Netherlands

ARTICLE INFO

Keywords:
Organic-inorganic supercrystalline nanocomposites
Generalized Maxwell's model
Inverse analysis
Statistically equivalent periodic unit cells

ABSTRACT

Supercrystalline nanocomposites, with their growing range of applications, present a significant challenge in understanding their structural behavior. These materials, composed of organically surface-functionalized inorganic nanoparticles arranged in periodic structures, exhibit superlattice imperfections, such as particle size scatter and superlattice vacancies, that emerge during fabrication. The mechanical effects of these defects, particularly particle size scatter and point defects, remain poorly understood due to experimental limitations. This study investigates these effects through advanced numerical modeling. A generalized Maxwell model is employed to model the oleic acid layer, with parameter values determined via inverse analysis. Subsequently, statistically equivalent periodic unit cells (SEPUCs) are used to simulate the impact of particle size scatter and point defects. Simulations reveal that nanocomposite mechanical properties, including stiffness, creep resistance, and plasticity, are highly influenced by particle distribution and the overlap volume of the organic interface. Conversely, point defects (superlattice vacancies) exhibit a negligible impact on the overall mechanical behavior. Furthermore, the material becomes increasingly isotropic with greater particle size scatter. These findings provide critical insights for the future design of these materials.

1. Introduction

In materials engineering, there has been an increasing focus on creating structurally ordered nanocomposites, among which supercrystalline nanocomposites are the most remarkable in terms of both achievable nanostructures and performance [1,2]. These sophisticated materials consist of inorganic nano-building blocks, typically surface functionalized with organic molecules, organized in periodic arrangements similar to those found in crystalline materials. Such supercrystalline arrangements are known as superlattices. The mechanical characteristics of these materials significantly surpass those of traditional hard polymers, and the consensus among researchers is that the superior mechanical properties, including strength, hardness, and stiffness, result from the supercrystalline arrangement together with organic ligands cross-linking [3–7]. The synthesis of durable inorganic–organic supercrystalline nanocomposites has attracted considerable attention recently [8]. A common method for their fabrication involves the self-assembly of surface-functionalized nanocrystals into orderly supercrystalline configurations, enabling precise control over their nano-features and potential interfacial interactions. Nonetheless, the forces that govern the self-assembly of nanobuilding blocks lose control at larger scales, leading to defects such as micro-cracks, superlattice vacancies, interstitials, dislocations, and precipitates [9]. These defects tend to become more pronounced as the size of the specimen increases, significantly impacting stiffness, strength, fracture toughness, etc., by several orders of magnitude [10,11].

Recent studies [12–14] have demonstrated the fabrication of face-centered cubic (FCC) supercrystalline nanocomposites composed of magnetite particles (Fe_3O_4), surface functionalized with oleic acid. They were synthesized through a sequential process of nanoparticle synthesis, self-assembly, pressing, and cross-linking-inducing heat treatment. The resulting supercrystalline nanocomposites displayed remarkable mechanical properties, particularly when heat-treated at higher temperatures (325 °C), due to an increased degree of cross-linking [14–16]. Although the nanocomposites achieved the closest possible packing, i.e., an FCC structure, they still contained defects, which led to

* Corresponding author at: Helmholtz Zentrum Hereon, Institute for Material Systems Modeling, Max–Planck-Straße 1, Geesthacht, 21502, Schleswig - Holstein, Germany.
E-mail address: vasu.kolli@hereon.de (V. Kolli).

https://doi.org/10.1016/j.mtcomm.2025.112924
Received 8 January 2025; Received in revised form 4 April 2025; Accepted 23 May 2025
Available online 10 June 2025

significant scatter in the microstructural tests conducted on the material [9,12,17]. The nanoscale structure of the samples posed significant challenges in controlling and assessing the effects of defects and particle size distributions. These factors are difficult to control in experimental settings, making it extremely challenging, if not impossible, to isolate and evaluate their individual effects on the overall mechanical behavior through experiments. Computational micromechanics offers a solution. Numerical modeling can quantify the contribution of key nanostructural features, especially superlattice defects and unavoidable particle size scatter, to the overall material behavior.

To date, various computational models have been applied to simulate the behavior of oleic acid supercrystalline nanocomposites. Li et al. [18] employed the Drucker–Prager elastoplastic model, while Ma et al. [19] adopted a non-local damage model based on micropolar continuum theory, aimed at exploring the inelastic and damage phenomena within the cross-linked organic interphases. Bor et al. [20] used a non-linear elastic material model to explain the tension–compression asymmetry evident in micro-cantilever beam bending tests. More recently, a generalized Maxwell model was used by the present authors to capture the time-dependent behavior of the nanocomposite [17]. All these approaches assumed a flawless FCC supercrystalline nanostructure, with uniform particle sizes and a defect-free particle arrangement. However, this assumption does not match well with the physical reality, as explained before.

The current research aims to develop a realistic model of supercrystalline oleic acid nanocomposites to study the effects of particle size scatter and point defects on overall mechanical behavior. To achieve this, a model was first established to describe the time-dependent material behavior of the individual components of the nanocomposite. Subsequently, the effects of particle size distribution and point defects on the macroscopic and time-dependent mechanical behavior of the material system were investigated. A numerical framework was implemented to study these aspects, which are difficult to manage experimentally. This study focused on particle size scatter and superlattice defects, specifically missing particles (superlattice vacancies). It is important to note that line, planar, or volume defects such as dislocations, stacking faults, twins, pores, or cracks were not addressed. Modeling these defects would require significantly larger microstructures (representative volume elements (RVEs)) or different modeling approaches, such as the discrete element method (DEM) [21,22]. Although not considered in this study, studying the mechanical effects of these defects represent a promising direction for future research.

This paper is organized as follows. Section 2 begins with a review of the material's processing techniques, microstructure, and previous constitutive modeling studies of homogenized nanocomposites that form the basis of the current work. The modeling framework is introduced in Section 3, which discusses the modeling of the microstructure and the constituent materials of the nanocomposite. The numerical analyses performed in the current study, namely the process of parameter identification for constitutive models for the nanocomposites' constituent materials and the influence of particle size scatter and point defects on overall material behavior, are presented in Section 4. The results and discussion are provided in Section 5, where the parameter values of the constitutive model of oleic acid are examined and validated, and the impact of particle size distribution and the role of point defects in affecting the nanocomposites' mechanical properties are analyzed. Finally, Section 6 summarizes the key findings, emphasizing the significance of oleic acid, particle size distribution, and point defects, and suggests directions for future research.

2. State of the art

This section presents the fundamental concepts necessary to understand the current work, including a summary of the material processing methods, the resulting microstructure, and previous modeling efforts that describe the homogenized material response of the nanocomposite.

2.1. Material processing

The material examined in this study was developed by the Institute of Advanced Ceramics at the Hamburg University of Technology as part of the collaborative project CRC 986 – Tailor-made multi-scale material systems. The material was fabricated through a sequential process involving nanoparticle synthesis, self-assembly, pressing, and heat treatment [12,14]. First, iron oxide (Fe_3O_4) nanoparticles were produced via the thermal decomposition of FeO(OH) in the presence of oleic acid at 320 °C in 1-octadecene, resulting in a suspension consisting of monodisperse nanoparticles approximately 15 nm in diameter. The oleic acid ($C_{18}H_{34}O_2$) acted as a surface functionalization agent, stabilizing the nanoparticles in suspension. These functionalized nanoparticles were then self-assembled into FCC superlattices through solvent evaporation or solvent destabilization methods [12,14] in die-punch assemblies. Once dried, the samples were pressed within the dies at 50 MPa and 150 °C, compacting the supercrystalline material into pellets while preserving their superlattice structures. The final step involved heat treatment at 325 °C in a nitrogen atmosphere, which induced cross-linking of the organic ligands via an oxidative radical polymerization reaction [16]. This process resulted in the formation of a covalent network throughout the organic phase, which is anchored to the nanoparticles, and caused mild shrinkage of the superlattice. For a detailed explanation of the sample preparation process, readers are referred to [12,14].

2.2. Microstructure

The resultant nanocomposite consisted of magnetite particles with a radius of 7–9 nm [12,14,20]. These particles were coated with an ultrathin layer of oleic acid with a thickness of approximately 1.1 nm [12,20]. The particles were arranged in a supercrystalline FCC structure (Fig. 1a) with a lattice constant of approximately 25 nm, as determined by SAXS measurements [9]. The inter-particle distance was thus calculated to be approximately 1.5 nm. The particle volume fraction was measured to be 57.5%. In many previous publications, e.g., [14,18–20], the particle size was assumed to be constant. However, more recently, Giuntini et al. [9] quantified the particle size scatter using a log-normal distribution with a mean radius of $\bar{r} = 8.1$ nm and a standard deviation of $r^{\sigma} = 1.3$ nm (Fig. 1c). In some cases, the particle size varied by more than 20%, resulting in "superamorphous" structures (Fig. 1b).

2.3. Constitutive modeling of homogenized nanocomposite

Although several earlier works [18,19] have modeled the material using elastoplastic models, the current study builds upon the author's previous work [17], which modeled the time-dependent material response of the homogenized supercrystalline oleic acid nanocomposite. The constitutive model used to capture the time-dependent material response is summarized in this section.

The previous work [17] modeled the time-dependent behavior of the entire homogenized supercrystalline magnetite oleic acid nanocomposite using a generalized Maxwell model. Generalized Maxwell models are implemented as a parallel rheological framework (PRF) [23] in the commercial finite element (FE) software ABAQUS® from Simulia, Dassault Systems [24]. In this framework, parallel finite-strain viscoelastic and elastoplastic networks contribute to the overall stress response. Each network is characterized by a decomposition of the deformation gradient into an elastic part and either a viscous or plastic part, depending on the network type. Plasticity within the plastic network is represented under finite strains using the von Mises yield criterion, without isotropic or kinematic hardening. The viscous response within the viscoelastic networks is governed by a flow rule, which can vary based on stress invariants and internal variables, along with an evolution law. The material response is assumed to be isotropic, and both plasticity and creep are considered to be isochoric.

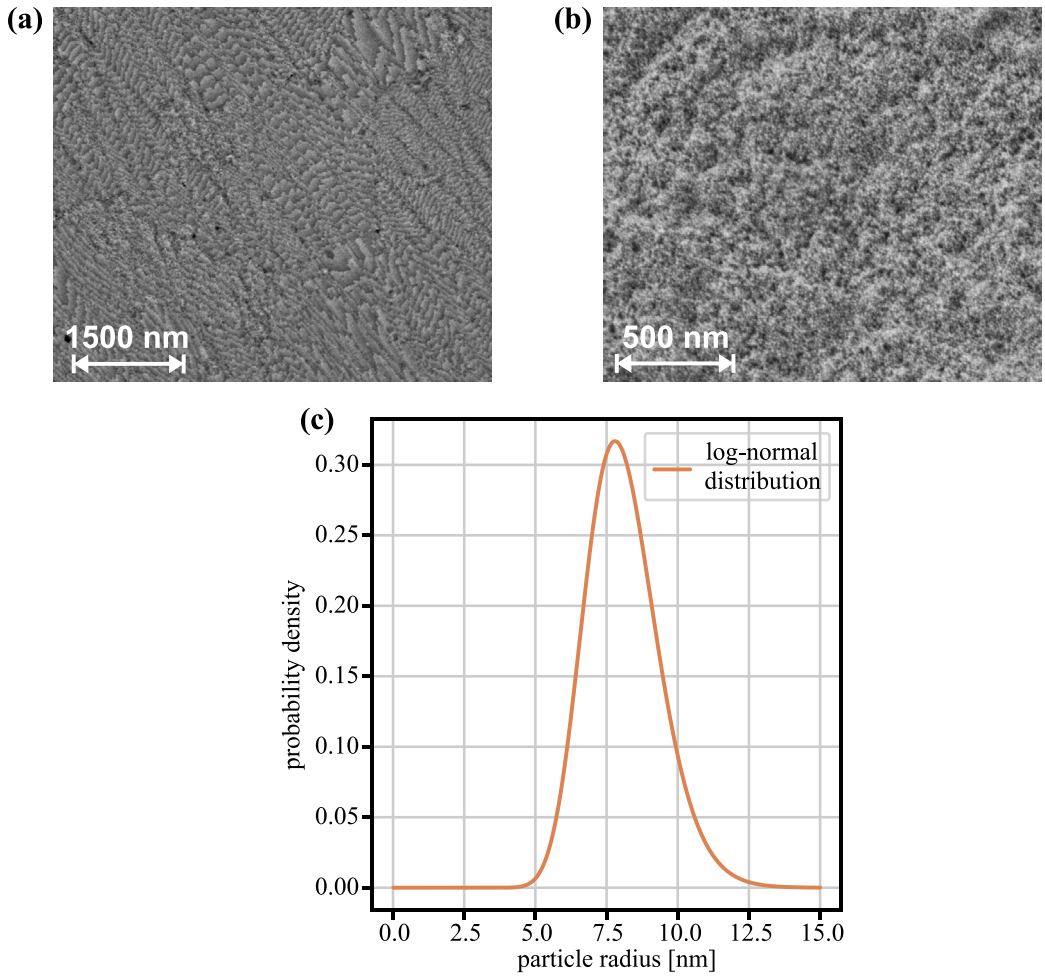

Fig. 1. Scanning electron microscope (SEM) images of self-assembled supercrystalline oleic acid nanocomposite samples with (a) crystallographic microstructure, (b) amorphous microstructure. (c) Log-normal distribution representing magnetite particles radii with mean 8.1 nm and standard deviation 1.3 nm.

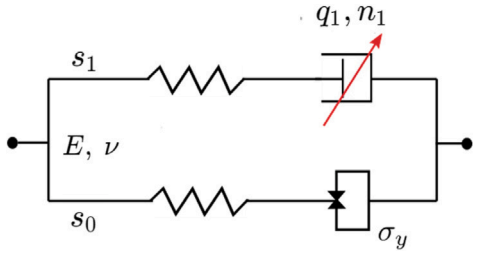

Fig. 2. ABAQUS® parallel rheological framework material model with one viscoelastic branch and one elastoplastic branch (1PRF model), where E is Young's modulus, ν is Poisson's ratio, σ_y is yield strength, s_0, s_1 are stiffness ratios, and q_1, n_1 are parameters of the creep stain evolution law described by Eq. (3).

The version of the generalized Maxwell model described in Kolli et al. [17] is shown in Fig. 2. This model, referred to as the "1PRF" model, consists of one elastoplastic equilibrium branch (network) and one viscoelastic branch (network). The stiffness ratios (s_0, s_1) in Fig. 2 represent the relative contribution of each network to the overall material response. Specifically, the total strain energy W^{tot} of the material is expressed as the weighted sum of the strain energies of the individual networks, as described by Eq. (1).

$$W^{\text{tot}} = \sum_{i=0}^{N} s_i W_i \tag{1}$$

where W_i is the strain energy of the ith network, and s_i is the stiffness ratio for the ith network, satisfying $\sum_{i=0}^{N} s_i = 1$.

The elastic strain energy of network i is given by Eq. (2).

$$W_i^e = s_i \left(\frac{E}{4(1+\nu)} (I_1 - 3) + \frac{E}{6(1-2\nu)} (J-1)^2 \right) \tag{2}$$

where W_i^e is the elastic strain energy of the ith network, E is Young's modulus, ν is Poisson's ratio, I_1 is the first invariant of the right Cauchy–Green strain tensor, and J is the determinant of the deformation gradient $\mathbf{F}$.

In [17], a simplified form of a power-law model was used to describe creep behavior, as represented by Eq. (3).

$$\dot{\bar{\varepsilon}}^{\text{cr}} = \left(\frac{\tilde{q}}{q_1} \right)^{n_1} \tag{3}$$

where $\dot{\bar{\varepsilon}}^{\text{cr}}$ is the equivalent creep strain rate, $\bar{\varepsilon}^{\text{cr}} = \sqrt{\frac{2}{3}\,\varepsilon^{\text{cr}} : \varepsilon^{\text{cr}}}$ is the equivalent creep strain, $\varepsilon^{\text{cr}} = \frac{1}{2}\ln(\mathbf{F}^{\text{cr}T}\mathbf{F}^{\text{cr}})$ is the logarithmic creep strain in terms of the creep deformation tensor $\mathbf{F}^{\text{cr}}$, $\tilde{q}$ denotes the equivalent deviatoric Kirchhoff stress, and q_1 and n_1 are the creep evolution material parameters of the (single) viscoelastic branch. Additionally, the plasticity parameter σ_y represents the yield strength.

The 1PRF model was used in Kolli et al. [17] to describe the time-dependent material response of the homogenized supercrystalline oleic acid nanocomposite. The values of the constitutive parameters for this model are provided in Table 1:

Table 1
Constitutive parameter values of the 1PRF model used to describe the time-dependent behavior of the homogenized supercrystalline oleic acid nanocomposite [17].

E [GPa]	ν	s_1	q_1 [MPa]	n_1	σ_y [MPa]
20.8	0.3	0.66	1385	3.4	805

3. Modeling framework

3.1. Microstructure

In this section, a similar representative volume element (RVE) to those used in previous studies [15,18,19] is introduced, where the nanocomposite is assumed to have a perfect FCC microstructure, without particle size scatter or defects. This is then expanded upon by discussing the modeling of microstructures that account for particle size scatter and superlattice vacancies.

3.1.1. Simplified model: regular microstructure

When assuming that the nanocomposite has a perfect supercrystalline FCC microstructure, without particle size scatter or defects, the resulting representative volume element (RVE) is a simple deterministic representative volume element (SDRVE) composed of an FCC unit cell with four magnetite particles coated with oleic acid, as illustrated in Fig. 3. Although this study primarily focuses on realistic microstructural modeling, the SDRVE is still employed for necessary simplifications in later sections (Section 3.2).

The finite element (FE) model was set up and meshed using the software Coreform Cubit™ [25]. The FE model consisted of an FCC unit cell with a lattice constant of 25 nm in all directions. The magnetite particles were modeled as spheres with a radius of 8.1 nm and placed in an FCC structure. An oleic acid layer of width 1.1 nm was modeled around each magnetite particle, resulting in a nearest neighbor distance (NND) of 1.475 nm. The model was meshed using a geometry-adaptive meshing scheme, with a maximum arc span of 7.5°, and employed three-dimensional continuum quadratic solid elements (ABAQUS® designation C3D10 [24]). The maximum arc span value of 7.5° was chosen to ensure that there were two layers of elements in the nearest neighbor region (Fig. 3). The resultant meshed model contained approximately 40,300 C3D10 elements.

The meshing was designed to ensure that opposite faces had identical surface meshes, facilitating the application of periodic boundary conditions (PBCs) during the FE simulation. PBCs are essential for accurately simulating the mechanical behavior of materials with repeating structures, such as composites and polycrystals. By applying PBCs, the analyzed RVE represents the entire material and tessellates seamlessly across space. This approach effectively extends the finite computational domain to an infinite medium, enabling the study of bulk material properties from a limited region. Henceforth, all FE models discussed in this study are designed with a mesh suitable for the application of PBCs.

3.1.2. Realistic model

When defects or particle size variations are considered in microstructure modeling, as in the current study, it becomes necessary to either use a larger representative volume element (RVE) or multiple microstructural units modified according to the statistical occurrences of these irregularities. In the literature, these larger RVEs that account for defects and particle size scatter are referred to as statistical volume elements (SVE), statistically similar volume elements (SSVE), or statistically equivalent periodic unit cells (SEPUC) [26–28]. In this study, they are referred to as SEPUCs, which are used to account for both particle size scatter and point defects. This subsection discusses the generation and meshing of these SEPUCs.

To represent the aforementioned particle size scatter and point defects in a modeling sense, it is important to consider a sufficient

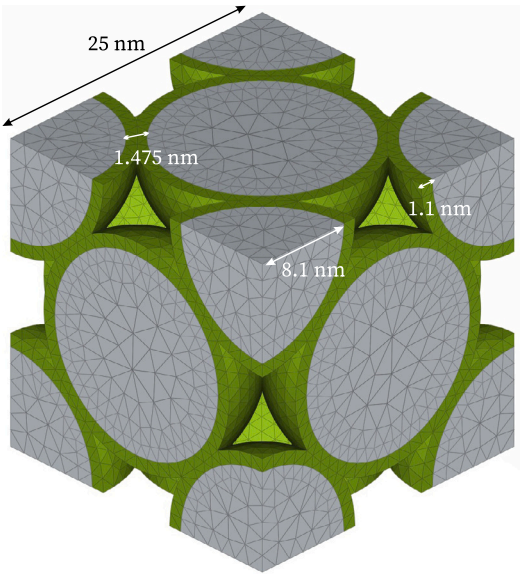

Fig. 3. Simple deterministic representative volume element (SDRVE) of supercrystalline oleic acid nanocomposite assuming perfect FCC microstructure.

number of particles. Due to computational constraints, there is a trade-off between the size of the RVE and the computational resources available. According to Schneider et al. [29], a RVE with around 100 particles is sufficient to capture effects of particle size distribution and point defects. In the present case, a model with 108 particles of radius $r = 8.1$ nm and volume fraction $v_f = 57.5\%$ was utilized. These 108 particles can form a perfect FCC microstructure made up of a $3 \times 3 \times 3$ RVEs as shown in Fig. 4a. This served as the starting point for the necessary modifications to incorporate particle size distribution and point defects.

Particle size distribution. Experimental measurements [9] indicated that the particle sizes follow a log-normal distribution, as shown in Fig. 1c. Due to the limitation of considering only a finite number of inclusions, it was not possible to match the intended log-normal distribution exactly. As a remedy, multiple realizations were generated for each configuration with a nominally equal distribution function, and the results were averaged. To this end, three different SEPUC configurations were investigated, as illustrated in Fig. 4.

Based on the original perfect FCC configuration (Fig. 4a), the first variation was a SEPUC with particle positions that were close to the perfect FCC positions, i.e., the underlying FCC structure was still present. However, the particle sizes followed the log-normal distribution shown in Fig. 1c. This SEPUC is henceforth referred to as the perturbed SEPUC, and a sample realization is shown in Fig. 4b. To achieve the perturbation, the Lubachevsky–Stillinger algorithm [30,31] was modified. This algorithm is an event-driven particle rearrangement algorithm [32] that allows the efficient and fast generation of random close packings of non-overlapping particles.

In the original implementation, particle centers were initially placed randomly, assigned velocities, and given growth rates. During the simulation, particles grew and interacted with one another through elastic collision events until the jamming limit was reached. For the perturbed SEPUC, the perfect FCC particle positions were used as the initial positions of each particle, with zero initial velocity, ensuring a certain degree of ordered structure. The growth rates of the particles were adjusted such that, after a specified simulation time of t_{end}, the particle radii increased to match the intended particle size distribution and inclusion volume fraction. During the growth process, particles growing faster than others came into contact with neighboring particles, causing

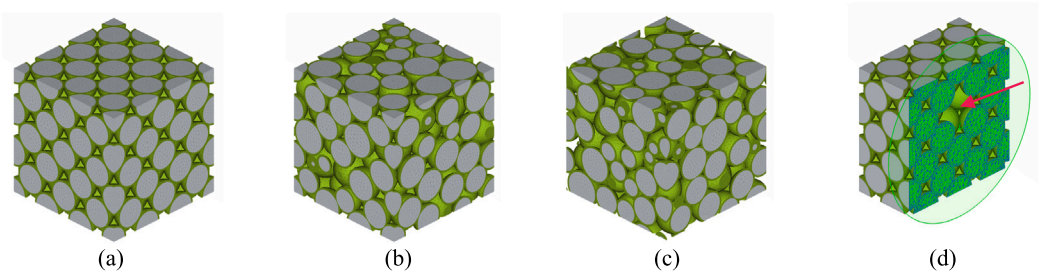

Fig. 4. Three different RVE configurations with a particle volume fraction of $v_f = 57.5\%$: (a) perfect FCC microstructure, (b) a sample realization of perturbed FCC SEPUC and (c) a sample realization of amorphous SEPUC (d) missing particle SEPUC cut into half with arrow pointing to the missing particle. While the perfect FCC and missing particle SEPUC variant has a constant particle size, the perturbed and amorphous SEPUCs have a log-normal size distribution with a mean value of 8.1 nm and a standard deviation of 1.3 nm.

them to move slightly. This process preserved a coarse FCC structure while maintaining the desired particle size distribution.

Although this variation of the Lubachevsky–Stillinger algorithm is well-defined, the final particle arrangement required verification for consistency. It was ensured that every particle maintained a nearest neighbor distance (NND) of 1.475 nm to its closest neighboring particle (where a "neighbor" is defined as a particle directly connected through oleic acid).

The second variation of the SEPUC was an amorphous SEPUC, characterized by a random particle arrangement (Fig. 4c). These SEPUCs were generated using the original Lubachevsky–Stillinger algorithm, which begins with randomized initial particle positions. The growth rate was adjusted to ensure that, by the end of the simulation time t_{end}, the desired particle size distribution and inclusion volume fraction were achieved. Care was taken to ensure that, despite the random initial placements, the arrangement of particles within the SEPUC remained periodic, similar to traditional RVEs.

To quantify and assess the order of randomness of the different SEPUC variants there exist many possibilities [33]. One of the most widely used approaches for statistically homogeneous and isotropic media, which is assumed here, investigates n-point correlation functions which give the probability of finding the same material phase (i) at n points that are apart by $\boldsymbol{r}_j$. To this end, it is instructive to introduce the indicator function $I^{(i)}$ of material phase (i) given by Eq. (4).

$$I^{(i)}(\mathbf{x}) = \begin{cases} 1 & \text{if } \mathbf{x} \text{ in material phase } i \\ 0 & \text{else} \end{cases} \tag{4}$$

which gives a complete description of the microstructural geometry information. The n-point correlation function is then given by Eq. (5).

$$S_n^{(i)}(\boldsymbol{r}_1 \dots \boldsymbol{r}_n) = \frac{1}{V} \int_{\Omega} \prod_{j=1}^{n} I^{(i)}(\mathbf{x} + \mathbf{r}_j)\, dV \tag{5}$$

whereas the 1-point correlation function simply gives the volume fraction of the respective phase i. To quantify the random character of a statistically homogeneous and isotropic microstructure, the 2-point correlation function is used, which gives the probability of two points separated by $\mathbf{r}$ belonging to the same material phase.

Thus far, the material consists of two phases: the particles, denoted as material phase (1), and the gaps between them, denoted as material phase (2). These phases satisfy the relation $I^{(1)}(\boldsymbol{x}) + I^{(2)}(\boldsymbol{x}) = 1$. The two-point correlation function can then be expressed as shown in Eq. (6).

$$S_2^{(1)}(\mathbf{r}) = \frac{1}{V_{\text{RVE}}} \int_{\Omega} I^{(1)}(\mathbf{x}) I^{(1)}(\mathbf{x} + \mathbf{r}_i)\, dV \tag{6}$$

For $\mathbf{r} = \mathbf{0}$ the 2-point correlation function $S_2^{(1)}(\mathbf{0}) = v_f$ gives the inclusion volume fraction of the particles. If the microstructure shows a completely random particle distribution, that is, no far-field ordering, the 2-point correlation function decays to a value of $S_2^{(1)} \to v_f^2$ with increasing distance $r = |\boldsymbol{r}|$. Fig. 5 depicts contour plots of slices of the 2-point correlation functions of the three SEPUC variants of Fig. 4. For the perfect FCC structure, a checkerboard pattern was observed. The two-point correlation function exhibited an oscillatory behavior, which was a clear indication of strong far-field order, as expected for a perfect FCC arrangement. The perturbed FCC SEPUC also displayed a checkerboard pattern; however, in comparison to the perfect FCC, this pattern was weakened. For increasing $\boldsymbol{r}$, the decaying regions of $S_2^{(1)}$ became wider. In contrast, the amorphous SEPUC did not exhibit any pattern-like contours in the two-point correlation function. The two-point correlation function decayed rapidly in all directions, indicating a fully randomized microstructure.

The statistical observations confirmed that the intended modeling approach was appropriate. It is important to note that, for the comparison of SEPUCs to be valid, the particle volume fraction was consistently maintained at $v_f = 57.5\%$. The described procedure was implemented in the programming language Python, making it fully automatable and enabling the generation of an arbitrary number of SEPUCs. For the purposes of this study, one realization of the perfect FCC structure and eight different realizations each of perturbed and amorphous SEPUCs were used.

Point defects. As mentioned in Section 1, the point defects considered in this study are superlattice vacancies, i.e., missing particles. The perfect FCC microstructure (Fig. 4a) was used as the starting point to generate SEPUCs with superlattice vacancies (missing particles).

Firstly, one particle was removed from the 108 particles in the perfect FCC structure. This SEPUC is henceforth referred to as the missing particle SEPUC (Fig. 4d). However, removing one particle out of 108 resulted in a reduction of the particle volume fraction by approximately 1%. This reduction did not allow for a reasonable comparison between SEPUCs. Therefore, a second SEPUC was generated, where the volume of the remaining particles was increased to compensate for the missing particle. This SEPUC is referred to as the missing particle SEPUC with correction. When visualized, this SEPUC appears very similar to the missing particle SEPUC shown in Fig. 4d, but with slightly larger particles. In summary, to study the effect of point defects, two types of SEPUCs were considered: the missing particle SEPUC and the missing particle SEPUC with correction.

After meshing, all SEPUCs consisted of approximately 450,000 tetrahedral elements with quadratic shape functions (ABAQUS designation C3D10). If the perfect FCC microstructure (Fig. 4a) were meshed with the same target element size as the SDRVE (Fig. 3), it would have contained more than 1,000,000 elements (20,200,000 nodes), resulting in considerable computational costs. Therefore, the target element size was doubled for all SEPUCs shown in Fig. 4. As a consequence of the coarser mesh, the simulation results of the perfect FCC microstructure (Fig. 4a) will differ slightly from those of the perfect FCC SDRVE (Fig. 3). It is also important to note that the meshing was performed in a manner that facilitates the application of periodic boundary conditions (PBCs).

3.2. Constitutive models of individual constituents

To investigate the effects of particle size scatter and point defects on the overall material behavior, it is essential to define constitutive models for the individual constituents of the nanocomposite.

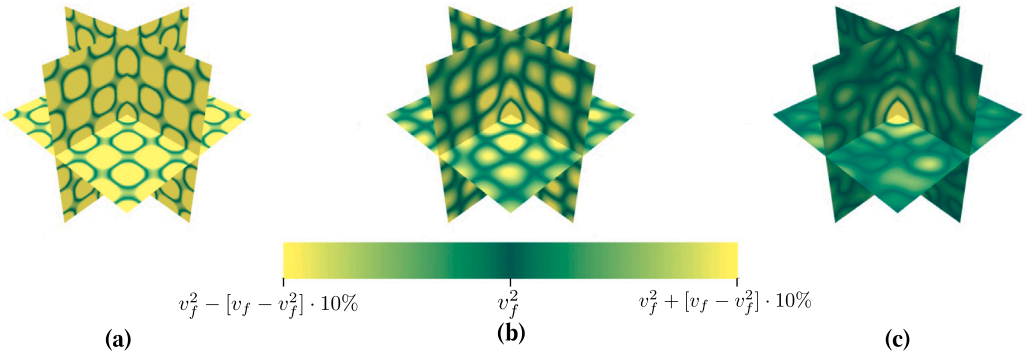

Fig. 5. Slices of contour plots of the 2-point correlation functions for the three different RVE variants containing 108 spherical inclusions: (a) perfect FCC particle arrangement, (b) perturbed FCC particle arrangement and (c) amorphous particle arrangement.

3.2.1. Magnetite nanoparticles

Previous studies [18,19] modeled the magnetite nanoparticles as a perfectly elastic material with a Young's modulus of 163 GPa and a Poisson's ratio of 0.3. This assumption is also adopted in the present study.

3.2.2. Oleic acid

Similar to the homogenized material behavior, previous studies [18, 19] have modeled oleic acid as a perfectly elastoplastic material with a Young's modulus of 13 GPa, a Poisson's ratio of 0.3 (or sometimes 0.49 for quasi-incompressibility), and a uniaxial tensile yield strength of approximately 900 MPa.

Building on the work presented in [17], where the homogenized material response was modeled using the 1PRF model shown in Fig. 2 (see also Section 2.3), the same model was applied to define the material response of oleic acid. A previous study [18] investigated the effect of the Poisson's ratio of oleic acid on the overall material behavior and determined that, for the homogenized material to exhibit a Poisson's ratio of 0.3, oleic acid must be modeled as a quasi-incompressible material ($\nu = 0.49$). Consequently, this assumption is adopted in the present study. The remaining constitutive parameters for oleic acid, namely the six parameters: Young's modulus (E), stiffness ratios (s_0, s_1), creep strain evolution parameters (q_1, n_1), and yield strength (σ_y), remain to be determined. This is discussed in the next section.

4. Numerical analysis

4.1. Parameter identification using inverse analysis

The process used to identify the 1PRF model parameters was the same as that employed in [17], referred to as "inverse analysis". Readers are encouraged to consult [17] for a more detailed understanding. In summary, the inverse analysis method utilizes an optimization algorithm and multiple iterations of FEM simulations to determine the best-fit material parameters for a given material model. This approach matches FEM simulation results to a reference solution (e.g., experimental data or other FEM simulations) by systematically adjusting the material parameters. Key elements of the procedure include selecting an appropriate optimization algorithm, defining the initial point and the error function, and establishing a stopping criterion for the iterative process.

This work employed the Nelder–Mead algorithm (as in [17]), and the error function used was the mean relative error (MRE), given by Eq. (7).

$$\mathrm{MRE} = \frac{1}{N}\sum_{t=t_1}^{t_N}\left|\frac{y_t^{\mathrm{hom}} - y_t^{\mathrm{SDRVE}}}{y_t^{\mathrm{hom}}}\right| \tag{7}$$

where, y is the output variable (stress or strain), the superscript hom, SDRVE denote homogeneous material and SDRVE respectively, and the subscript t denotes the simulation time. When the MRE did not improve by more than 10^{-3} from the previous iteration, the minimum was assumed to be reached.

In the present study, an iterative comparison was performed between a FEM simulation of a load case on the homogenized material, characterized by the material parameters listed in Table 1, and a corresponding FE model of an RVE representing the nanocomposite. During each iteration, the constitutive parameter values were updated to minimize the difference between the two models. To conduct the inverse analysis, FE models were required for both the homogenized material and the nanocomposite. The homogenized material was represented as a unit cube composed of a single finite element. Conversely, representing the nanocomposite using an RVE that captures its microstructure, including particle size scatter and point defects as shown in Fig. 4b, was computationally impractical due to the high number of simulations required for the inverse analysis. To improve the feasibility of the inverse analysis, two simplifications were applied:

Simplified model. It was assumed that the nanocomposite possessed a perfect FCC microstructure without particle size scatter or defects. This assumption implied that the geometry could be represented by the SDRVE discussed in Section 3.1.1.

Simplified constitutive modeling. Simplified constitutive modeling [34–37] involves the use of reduced or simplified mathematical models to describe material behavior under various loading conditions. These models typically employ fewer parameters and are less complex compared to more detailed models, such as the 1PRF model. The primary goal is to capture specific mechanical responses of the material, such as elasticity, elastoplasticity, or viscoelasticity, individually, thereby enhancing computational efficiency. In this approach, the constitutive model is divided into its three fundamental types of behavior: elasticity, plasticity, and viscosity. The 1PRF model (Fig. 2) was simplified using simplified constitutive models (SCMs) by selectively deactivating viscosity and/or plasticity components as needed.

In ABAQUS, simplified constitutive models (SCMs) of any constitutive model can be created by modifying the material definition and/or analysis type. The use of SCMs not only reduces the computational time for individual SDRVE FE simulations during each iteration but also decreases the total number of iterations required to reach a solution. This is achieved by reducing the number of parameters, thereby simplifying the parameter space. Moreover, this approach improved the uniqueness of the solution obtained via inverse analysis, addressing a significant challenge encountered in [17].

Preliminary results indicated that simplifying the 1PRF model by deactivating both viscous and plastic effects (elastic SCM) reduced the SDRVE FE simulation time for a load case to only 15 minutes, compared to 20 hours when using the full-scale 1PRF model. Furthermore, removing only the viscous effects resulted in an SDRVE FE simulation with the elastoplastic SCM that required just 1 hour to complete. These

results demonstrated that the combined use of the SDRVE and SCMs significantly improved the feasibility of inverse analysis.

Inverse analysis is generally conducted by iteratively comparing experimental results with their corresponding FE simulations. Consequently, SCMs cannot typically be employed in general cases, as perfect isolation of elastic, viscous, and plastic effects selectively through nanoscale experiments is not feasible. However, in the present study, two FEM simulations were compared: the FE simulation of a homogenized material model (unit cube) and the SDRVE model (Fig. 3). This approach facilitated a comparison of the FE simulation of the homogenized material model (unit cube) with the SDRVE model, both equipped with the same SCM, instead of the full-scale 1PRF model. This adjustment made the comparison computationally viable. As a result, instead of performing inverse analysis directly on the SDRVE and homogenized models using the full-scale 1PRF model, the process was divided into three separate steps.

In the first step (Step 1), inverse analysis was conducted to determine the value of the elastic parameter, specifically Young's modulus (E), by iteratively comparing FE simulations of the SDRVE and the homogenized material FE model (unit cube). Both models were equipped with an elastic SCM (excluding viscosity and plasticity) instead of the full-scale 1PRF model. The FE simulations using the elastic SCM are referred to as elastic simulations. The elastic simulations were displacement-controlled and subjected to uniaxial loading up to a strain of ε_{11} and ε_{12} equal to 0.05 for tension and shear, respectively, as illustrated in Fig. 6a. The mean relative error (MRE) was calculated for the stress values ($y = \sigma_{11}$) at the end of the simulation ($t_1 = 10$ seconds).

In the second step (Step 2), Young's modulus (E) was set to the value obtained in Step 1, and the optimization was performed for the stiffness ratio (s_1) and creep evolution parameters (q_1, n_1). The stiffness ratio s_0 was not considered explicitly, as it was calculated using the equation $s_0 = 1 - s_1$. A simplified constitutive model (SCM) without plasticity, referred to as the viscoelastic SCM, was used, and the corresponding FE simulations are termed viscoelastic simulations. The viscoelastic simulations were conducted in a force-controlled manner. A stress rate of 15 MPa/s was applied to the RVE up to a maximum stress of $\sigma_{11} = 150$ MPa. The stress was then held constant for 1000 seconds. Subsequently, the RVE was loaded to $\sigma_{11} = 250$ MPa at a rate of 10 MPa/s, followed by another 1000 seconds of stress hold. Finally, the RVE was loaded to $\sigma_{11} = 350$ MPa at a rate of 5 MPa/s and held at this stress level for 1000 seconds. The input loading regime is depicted in Fig. 6b. The mean relative error (MRE) was calculated for the strain values ($y = \varepsilon_{11}$) at selected times: $t_1 = 10$, $t_2 = 110$, $t_3 = 1010$, $t_4 = 1020$, $t_5 = 1120$, $t_6 = 2020$, $t_7 = 2040$, $t_8 = 2140$, and $t_9 = 3040$ s.

Finally, the third step (Step 3) of the inverse analysis was conducted to determine the value of the plasticity parameter, specifically the yield strength (σ_y), using an elastoplastic SCM (excluding viscous effects). The constitutive parameters E and s_1, obtained from the previous steps, were already set as constants in the elastoplastic SCM. Following the established naming convention, the FE simulations using the elastoplastic SCM are referred to as elastoplastic simulations. In the elastoplastic simulations, the FE geometry was deformed uniaxially until a strain of 0.15 was reached. Subsequently, the displacement boundary condition was removed, allowing the material to recover freely until it reached its residual strain, as illustrated in Fig. 6c. In the context of this study, the permanent deformation remaining in the material after complete unloading is referred to as residual strain. For the elastoplastic simulations, the mean relative error (MRE) was calculated for the residual strain ($y = \varepsilon_{11}$) at the end of the simulation ($t_1 = 5.1$ seconds).

The order of the inverse analysis steps is crucial because the yield strength (σ_y) depends on the value of the stiffness ratio (s_1), and, in turn, all viscous parameter values (s_1, q_1, n_1) depend on the elastic material parameters (E, ν). Therefore, to ensure the accuracy of the solution, the order outlined above was followed. The results of this three-step inverse analysis are presented in Section 5.1.

4.2. Mechanical properties of statistically equivalent periodic unit cells

Three key properties of SEPUCs were analyzed: viscoelasticity, elastoplasticity, and anisotropic elasticity. Viscoelasticity and elastoplasticity were studied through simulations conducted using simplified constitutive models (SCMs). These SCMs were generated following the methodology described in Section 3.1.2. The objective of this analysis was not only to minimize computational costs but also to distinctly evaluate the effects of particle scatter and point defects on viscous and plastic behaviors separately.

The influence of particle scatter and point defects on the anisotropy of supercrystalline oleic acid nanocomposites was investigated by assessing a property called "anisotropic elasticity", which describes the variation in elastic properties of a material depending on the direction of the applied force or deformation. This characteristic is typical of crystalline materials, where the atomic arrangement influences the material's response to mechanical stresses in different directions. In this study, the concept of anisotropic elasticity was extended to supercrystalline nanocomposites to analyze their anisotropy. The anisotropy of cubic crystals (also referred to as cubic symmetry) can be quantified using a dimensionless parameter called the anisotropic factor or Zener ratio (a_r). For FCC crystals with cubic symmetry, the Zener ratio (a_r) can be expressed in terms of Young's modulus (E), shear modulus (G), and Poisson's ratio (ν), as shown in Eq. (8).

$$a_r = \frac{2G(1+\nu)}{E} \tag{8}$$

This formulation provides insights into the degree of anisotropy, where $a_r = 1$ indicates isotropic behavior, and values deviating from 1 represent increasing levels of anisotropy.

Initially, in the viscoelastic simulations, a simplified constitutive model (SCM) excluding plasticity was employed. Each of the eight perturbed and eight amorphous SEPUCs was subjected to a uniaxial tensile stress σ_{11} of 350 MPa, applied over 10 seconds in the X-direction. Following this initial loading phase, the stress was held constant for 1000 seconds to observe creep behavior. Subsequently, the SEPUC was unloaded over a period of 1 second and allowed a recovery period of 1000 seconds. The entire loading history, encompassing these phases, is detailed in Fig. 7a.

In the elastoplastic simulations, a simplified constitutive model (SCM) excluding viscous effects was employed. The SEPUCs were subjected to a uniaxial tensile strain of $\varepsilon_{11} = 0.15$ in the positive X-direction, uniformly applied over 5 seconds. Following this loading, the displacement boundary condition was removed, allowing the SEPUCs to stabilize and reveal any residual strain. Given the absence of viscous effects, the loading and unloading rates did not influence the simulation outcomes. This loading sequence is detailed in Fig. 7b.

To analyze the anisotropic elasticity of all SEPUCs (Fig. 4), the respective Zener ratios were calculated. The values of Young's modulus (E) and Poisson's ratio (ν) were determined through a uniaxial tension simulation of a SEPUC, employing a displacement boundary condition to achieve 1% tensile strain (ε_{11}) and an elastic simplified constitutive model (SCM). The shear modulus (G) was obtained from a pure shear simulation of a SEPUC, using an elastic SCM with a displacement boundary condition that induced 1% shear strain (ε_{12}). For the purposes of this analysis, these tensile and shear simulations are collectively termed anisotropic simulations. Finally, the Zener ratio (a_r) was calculated using the formula provided in Eq. (8). The results of all the SEPUC simulations are presented in Section 5.2.

It is important to note that the perfect FCC microstructure exhibits the highest stiffness along the ⟨111⟩ direction. However, in this investigation, the ⟨100⟩ direction, which represents the weakest orientation, was selected for loading. Given that the fabricated nanocomposite typically comprises multiple grains with varying orientations, understanding the strength of the material's weakest link is crucial for material design. Therefore, uniaxial loading along the ⟨100⟩ direction was chosen for this analysis.

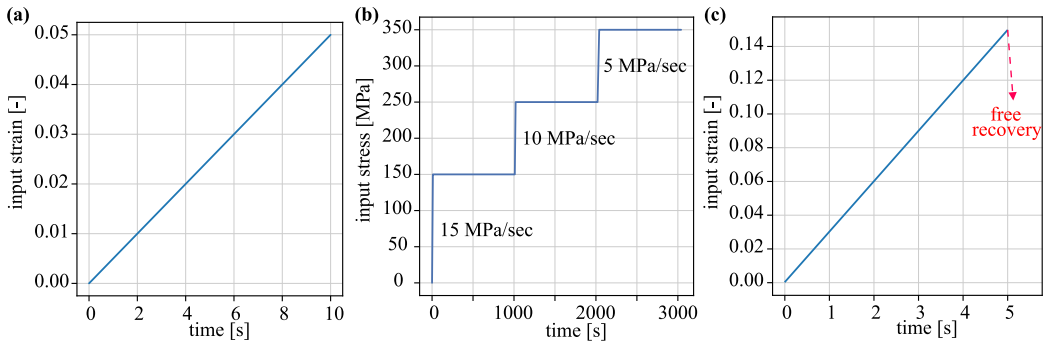

Fig. 6. Input boundary conditions for FE simulations in the three steps of inverse analysis: (a) Input strain history for elastic simulations in step - 1, (b) Input stress history for viscoelastic simulations in step - 2, and (c) Input strain history for elastoplastic simulations in step - 3. For elastoplastic simulations, the strain is removed after 5 s and the material is allowed to recover freely after removing the displacement BCs. This is shown by the red arrow.

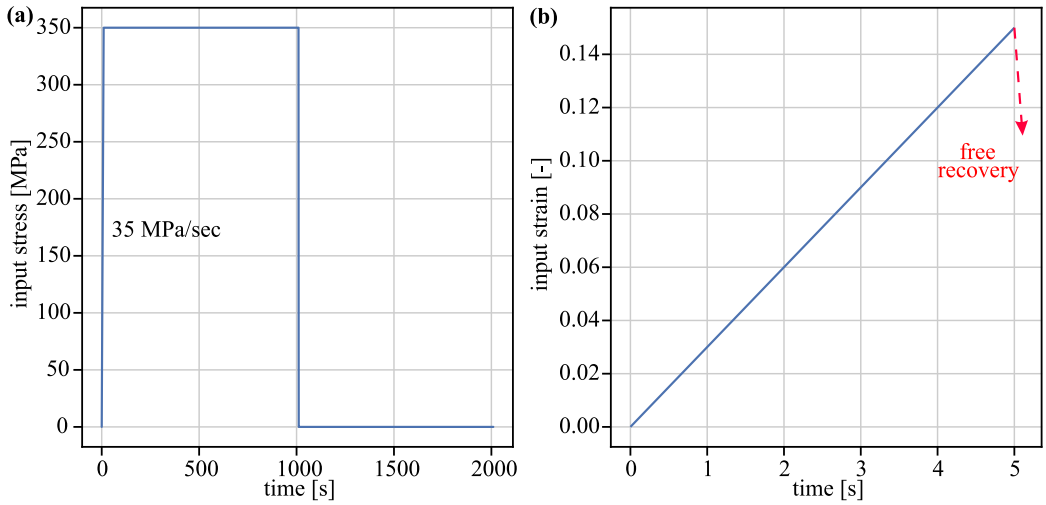

Fig. 7. (a) Input uni-axial tensile stress (σ_{11}) history for viscoelastic simulations, (b) Input uni-axial tensile strain (ε_{11}) history for elastoplastic simulations. For elastoplastic simulations, the displacement BCs are removed at the end of 5 s to allow for free material recovery in order to identify the residual strain.

Table 2
Oleic acid material parameter values of 1PRF model obtained by performing inverse analysis in three separate steps.

E [GPa]	ν	s_1	q_1 [MPa]	n_1	σ_y [GPa]
11.69	0.49	0.66	4663	2.49	1.5

5. Results and discussion

5.1. Parameter identification using inverse analysis

The material parameters obtained from the three inverse analyses, utilizing different simplified constitutive models (SCMs), are tabulated in Table 2. The mean relative error (MRE) values at the conclusion of the inverse analyses, using elastic, viscoelastic, and elastoplastic SCMs, were 0.205, 0.01248, and 3.71×10^{-5}, respectively. These low MRE values indicate a strong agreement between the homogeneous and the stochastic discrete representative volume element (SDRVE) macroscopic material behavior. This close agreement of the output stress/strain histories from the SDRVE finite element simulation, employing the constitutive parameter values obtained from the inverse analyses, is illustrated in Fig. 8.

The Young's modulus (E) of 11.69 GPa aligns with the expected range cited in the literature [9,12,18,19]. From Fig. 8a, it is evident that the larger error in the elastic simulation stems from an underestimation of the tensile response, while the shear response exhibits a stiffer behavior than that of the homogeneous material. This discrepancy arises due to the neglect of cubic symmetry when modeling the oleic acid. As will be discussed in Section 5.2.3, this symmetry can be neglected if the FCC structure is imperfect due to particle size scatter.

A stiffness ratio $s_1 = 0.66$ for the viscoelastic branch indicates significant time-dependent behavior of the oleic acid, which was anticipated given the time-dependent nature of the homogenized material. The yield strength for oleic acid (σ_y) was determined to be 1.5 GPa. It is important to note that the yield strength of the homogeneous material (Table 1) had been estimated to be 805 MPa [17]. The discrepancy between these two values is attributable to two primary factors: (1) Plasticity was not modeled in the magnetite particles, thereby necessitating that all plastic deformation occur within the oleic acid, and (2) The oleic acid possesses a lower cross-sectional area than the homogeneous material, which was typically modeled as a unit cube, resulting in higher stresses for the same strain in the oleic acid. Consequently, for the SDRVE to exhibit the same plastic strain as the homogeneous material, the yield strength of oleic acid must be higher than 805 MPa. Previous modeling studies [18,19] have reported a yield strength of 900 MPa for oleic acid (as opposed to the 1.5 GPa obtained here) because they modeled the material as an elastoplastic material, without accounting for viscosity. The superior properties of cross-linked oleic acid have been documented in previous experimental studies, demonstrating the significant impact of cross-linking on the overall mechanical behavior of these nanocomposites. Cross-linking alone has been shown to consistently increase the Young's modulus of the nanocomposite by over 200% [9,12,14,15,20,38]. Therefore, the high yield strength observed is justified.

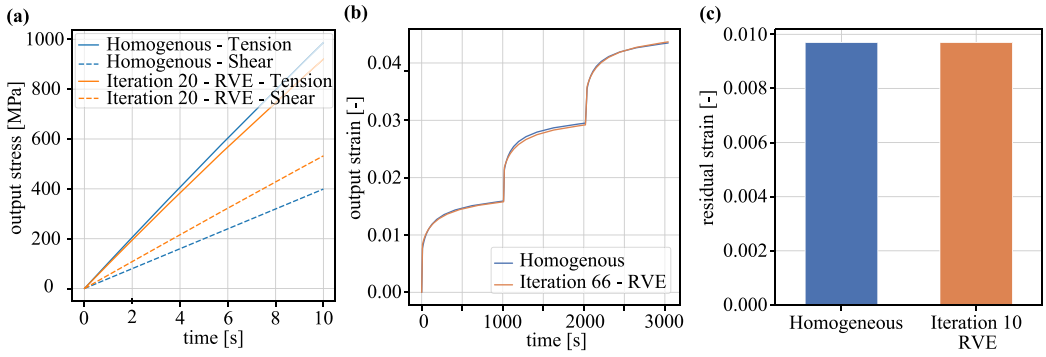

Fig. 8. Simulation results using the final constitutive parameter set derived by conducting inverse analysis in three separate steps: (a) Output stress history for step - 1 (elastic simulations), (b) Output strain history for step - 2 (viscoelastic simulations), and (c) Residual strain for step - 3 (elastoplastic simulations), of homogenized supercrystalline oleic acid nanocomposite FE model (unit cube) and SDRVE FE model.

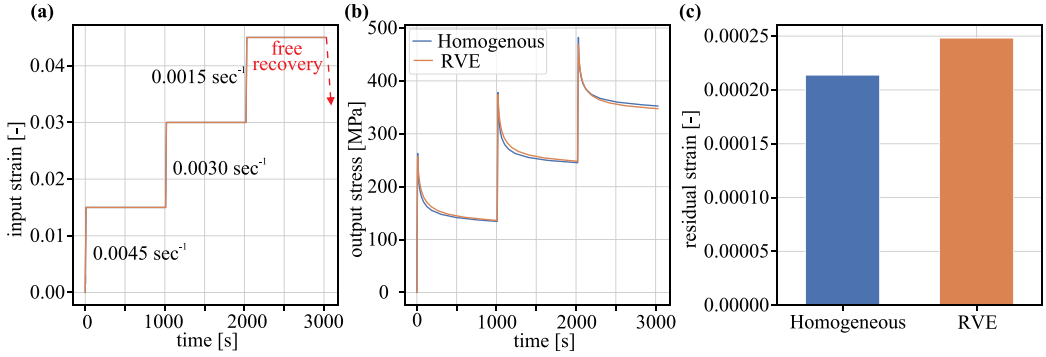

Fig. 9. Validation load case of a SDRVE FE simulation with 1PRF model (Fig. 2): (a) Input strain history till 3030 seconds and a red arrow showing free recovery (b) Output stress relaxation curve till 3030 seconds, and (c) Residual strain at the end of relaxation time of 10^6 seconds.

To validate the constitutive parameter values and assess the effectiveness of performing inverse analysis in three steps with the stochastic discrete representative volume element (SDRVE) and simplified constitutive models (SCMs), a validation load case was simulated with a full-scale 1PRF model. Additionally, to further evaluate the robustness of the obtained material parameter values, as opposed to the force-controlled simulations used in Section 4.1 (viscoelastic simulations), displacement-controlled simulations were performed, and the stress relaxation curves and residual strain were compared between the homogeneous and SDRVE finite element models. To this end, the material was initially loaded uniaxially to a strain of $\epsilon_{11} = 0.015$ at a rate of 0.0045 s^{-1}, and then the strain was held constant for 1000 s. Subsequently, the strain ϵ_{11} was increased to 0.03 at the rate of 0.0030 s^{-1} and maintained for another 1000 seconds. Finally, the strain was further increased to 0.045 at the rate of 0.0015 s^{-1}, and was once again held constant for 1000 seconds. After completing these stages, the displacement boundary condition (BC) was removed, allowing the material to settle into its final state with a relaxation simulation time of 10^6 seconds. The input strain history for this process is depicted in Fig. 9a. The simulation results for this validation load case are illustrated in Figs. 9b and 9c. The mean relative error (MRE), calculated using Eq. (7) for the stresses at simulation times t_i - 10, 110, 1010, 1020, 1120, 2120, 2130, 2230, and 3030 seconds (Fig. 9b) and for the residual strain at 10^6 seconds (Fig. 9c), was 0.0319. This low MRE not only validates the robustness of the constitutive parameters identified but also demonstrates the effectiveness of conducting inverse analysis using computationally inexpensive SCMs in three stages, as opposed to using a computationally expensive full-scale 1PRF model.

5.2. Mechanical properties of statistically equivalent periodic unit cells

This section reports the results of the simulations of SEPUCs as described in Section 4.2. Specifically, the simulations include the perfect FCC structure, eight realizations of perturbed SEPUCs, eight realizations of amorphous SEPUCs, the missing particle SEPUC, and the missing particle SEPUC with correction.

5.2.1. Viscoelasticity

The time-dependent mechanical properties of SEPUCs are strongly influenced by their structural configuration. As shown in Fig. 10a, the creep strain evolution between $t = 10$ seconds and $t = 1010$ seconds differs significantly. Amorphous SEPUCs exhibited greater creep resistance (lower creep strain) compared to perturbed SEPUCs, which, in turn, outperformed the perfect FCC microstructure. Based on the mean curves and the scatter bands therein, it is evident that all eight realizations of the amorphous SEPUCs exhibited less creep than the eight perturbed SEPUCs, which, in turn, exhibited less creep than the perfect FCC microstructure. Regarding the effect of superlattice vacancies, Fig. 10b indicates that the missing particle SEPUC with correction demonstrated greater creep resistance compared to the perfect FCC microstructure, followed by the missing particle SEPUC.

These trends in the mechanical properties of SEPUCs can be primarily attributed to variations in oleic acid overlap volume within the SEPUCs. Numerically, an increase in oleic acid overlap volume results in a larger effective cross-sectional area, which in turn reduces the overall macroscopic creep strain of a SEPUC under a given uniaxial tensile stress. Experimentally, the overlap volume has been a key factor in determining the extent of oleic acid chain cross-linking during the heat treatment process. Greater overlap volume promotes more extensive cross-linking between particles through the interdigitation of

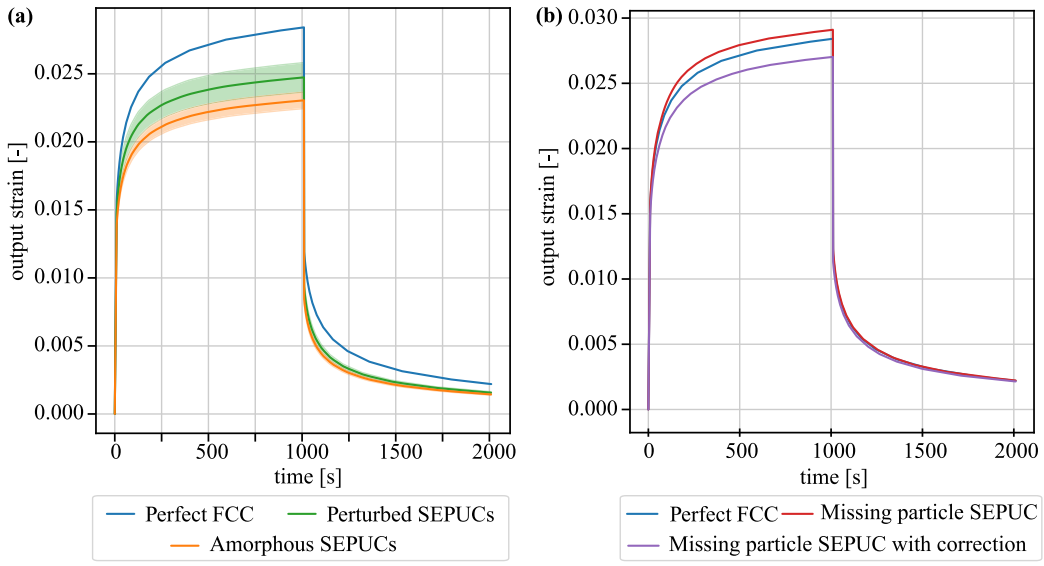

Fig. 10. (a) Output strain history of perfect FCC, perturbed SEPUCs (average with standard deviation), amorphous SEPUCs (average with standard deviation), (b) Output strain history of perfect FCC, missing particle SEPUC and missing particle SEPUC with correction.

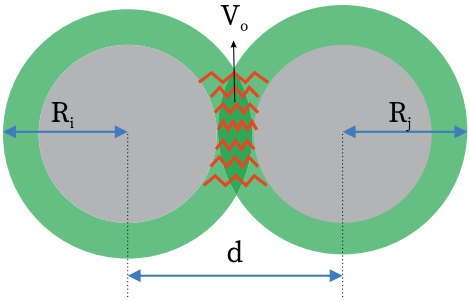

Fig. 11. Oleic acid overlap of two magnetite particles surface functionalized with oleic acid with outer radii R_i and R_j, with centers separated by a distance d. The red lines represent the cross-linked oleic acid chains after heat treatment which are a function of overlap volume.

the oleic acid ligands' aliphatic chains, thereby enhancing the creep resistance of the SEPUC structures. The overlap volume between two spheres, each with radii R_i and R_j as shown in Fig. 11, is quantitatively described by Eq. (9).

$$V_o\left(R_i, R_j\right) = \frac{\pi}{12d}\left(R_i + R_j - d\right)^2\left(d^2 + 2d\left(R_i + R_j\right) - 3\left(R_i - R_j\right)^2\right) \tag{9}$$

where, d represents the distance between the centers of the two spheres with radii R_i, R_j. The total oleic acid overlap volume for a SEPUC (V_o^{tot}) is calculated using Eq. (10).

$$V_o^{tot} = \sum_{i,j} V_o\left(R_i, R_j\right) \qquad \forall \quad R_i + R_j > d \tag{10}$$

where d represents the distance between the centers of the two spheres with radii R_i, R_j. To ensure a fair comparison across different SEPUCs, normalized oleic acid overlap volume (V_o^n) is calculated by dividing the total oleic acid overlap volume (V_o^{tot}) of a SEPUC (given by Eq. (10)) by its total volume (V_{SEPUC}) as shown in Eq. (11).

$$V_o^n = \frac{V_o^{tot}}{V_{\text{SEPUC}}} \tag{11}$$

The total volume of a SEPUC is given by Eq. (12).

$$V_{\text{SEPUC}} = \left[\sum_k \frac{4}{3}\pi R_k^3\right] - V_o^{tot} \tag{12}$$

where, R_k is the surface functionalized magnetite particle radius and V_o^{tot} is the total oleic acid overlap volume of the SEPUC. The normalized oleic acid overlap volume (in percentage) for all SEPUCs is presented in Fig. 12.

Amorphous SEPUCs exhibited a higher normalized overlap volume, V_o^n, than perturbed SEPUCs, followed by the perfect FCC structure, as illustrated in Fig. 12a. Consequently, under a given uniaxial tensile stress, σ_{11}, amorphous SEPUCs demonstrated greater creep resistance than perturbed SEPUCs, followed by the perfect FCC structure, as shown in Fig. 10a. This correlation with V_o^n is also evident in SEPUCs with superlattice vacancies. For the same uniaxial tensile stress, σ_{11}, the missing particle SEPUC, with a particle volume fraction of 56.5%, exhibited lower creep resistance than the perfect FCC structure, with a particle volume fraction of 57.5%, due to a reduction in V_o^n caused by the missing particle, as shown in Figs. 10b and 12b. In contrast, the missing particle SEPUC with correction demonstrated higher creep resistance than the perfect FCC structure, under a given uniaxial stress, σ_{11}. Although both structures had the same particle volume fraction of 57.5%, the missing particle SEPUC with correction had a higher V_o^n due to the increased particle size. Thus, oleic acid overlap plays a significant role in the structural integrity of the nanocomposite.

5.2.2. Elastoplasticity

The expected behavior of elastoplastic simulations on particle size distributed SEPUCs is that the perfect FCC structure would exhibit the highest residual strain, followed by perturbed SEPUCs, and then amorphous SEPUCs, due to the influence of the oleic acid overlap volume. It is generally understood that a higher overlap volume under the same strain should result in higher elastic strain energy and, consequently, reduced residual strain. However, observations contradicted these expectations, as shown in Fig. 13a. Surprisingly, perturbed SEPUCs exhibited the lowest mean value of residual strain, followed by amorphous SEPUCs, and then the perfect FCC structure, effectively reversing the anticipated order of amorphous and perturbed SEPUCs. Furthermore, a large standard deviation was observed for the amorphous SEPUCs; specifically, the lower limit of residual strain (ε_{11} at the end of simulation) is lower than that of the perturbed SEPUCs, and the upper limit is higher than that of the perfect FCC structure.

This anomaly can be attributed to the distribution of oleic acid across particles within the SEPUC. In a perfect FCC microstructure, each particle is directly connected to 12 neighboring particles (defined as those linked through oleic acid), resulting in a uniform distribution of

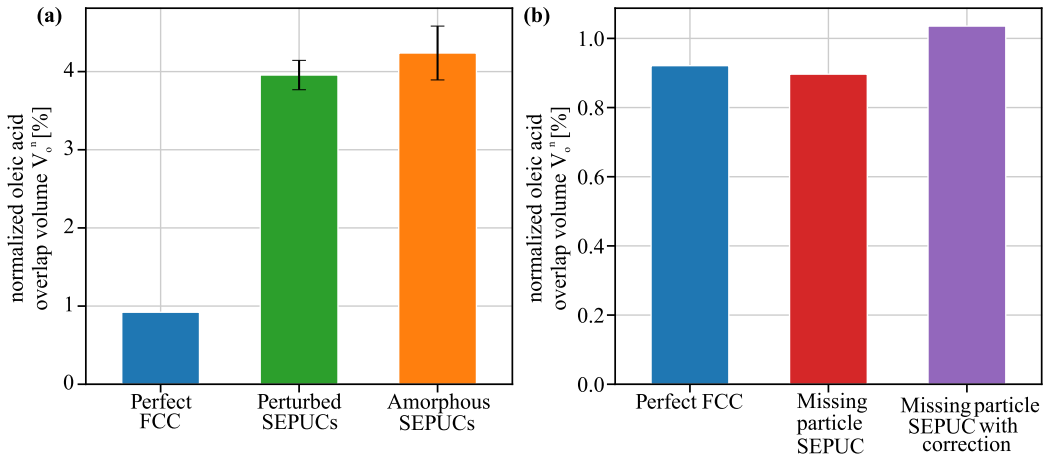

Fig. 12. Normalized oleic acid overlap volume (V_o^n) given by Eq. (11) (in percentage) of (a) Perfect FCC, perturbed SEPUCs (average with standard deviation), amorphous SEPUCs (average with standard deviation), (b) perfect FCC, missing particle SEPUC and missing particle SEPUC with correction.

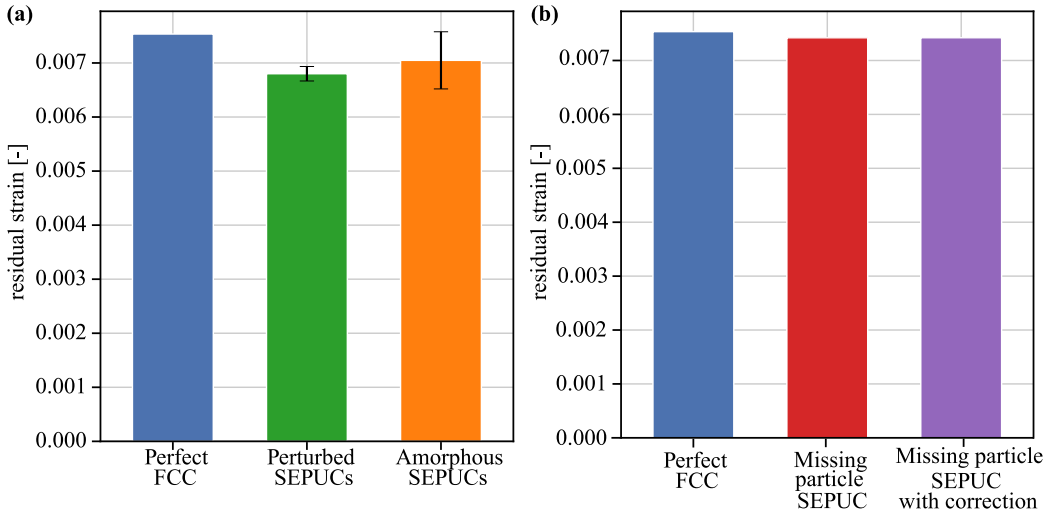

Fig. 13. Residual strain (ε_{11} at the end of simulation) in the elastoplastic simulation, Fig. 7. (a) Comparison of perfect FCC microstructure, perturbed SEPUCs (average with standard deviation), amorphous SEPUCs (average with standard deviation), (b) Comparison of perfect FCC microstructure, missing particle SEPUC and missing particle SEPUC with correction.

the oleic acid. In contrast, perturbed SEPUCs have an average of 11.75± 0.032 neighbors per particle across eight realizations, which is slightly fewer than in the perfect FCC structure. This decrease is due to a few particles with smaller radii that did not form oleic acid-mediated connections with neighboring particles. Consequently, perturbed SEPUCs exhibit less residual strain than the perfect FCC structure due to their higher V_o^n, as the oleic acid volume is relatively uniformly distributed within each perturbed SEPUC and, hence, does not significantly affect the residual strains. However, the effect of oleic acid overlap volume distribution is more pronounced in amorphous SEPUCs, leading to their erratic behavior. Amorphous SEPUCs exhibit greater variability, with an average of 11.5 and a large standard deviation of 0.101 neighbors per particle across eight realizations. It is observed that some particles in certain amorphous SEPUC realizations have as few as five neighbors, leading to an early onset of high stresses and thus higher residual strain. Simultaneously, there are also some amorphous SEPUC realizations with a more uniform oleic acid distribution exhibiting the lowest residual strain across all SEPUCs. Despite having a higher V_o^n than both perturbed SEPUCs and the perfect FCC structure, the variability in oleic acid overlap across different amorphous SEPUC realizations leads to a larger standard deviation in residual strain, as shown in Fig. 13a. Overall, this highlights the critical role of particle distribution in determining the mechanical behavior of SEPUCs.

The impact of point defects on the elastoplastic behavior of SEPUCs revealed further unexpected results. Conventionally, it is anticipated that SEPUCs with a missing particle would exhibit a higher residual strain compared to a perfect FCC microstructure due to the introduction of a missing particle. However, contrary to the expected behavior, it was found that the perfect FCC structure actually displayed a slightly higher residual strain than the missing particle SEPUC, as shown in Fig. 13b. This counter-intuitive finding can be explained by the slight redistribution of particles around the point defect during the unloading phase of the simulation. Although the missing particle SEPUC undergoes more plastic deformation, especially around the void, the neighboring particles adjust by slipping slightly into the void of the missing particle during unloading. This small movement effectively reduces the residual strain further, illustrating a complex interplay of structural rearrangement and mechanical response in SEPUCs with point defects.

Even for the case of the missing particle SEPUC with correction, the residual strain is a result of the interplay between increased oleic acid overlap volume (Fig. 12b) due to an increase in particle size and particle rearrangement due to the void caused by the missing particle. However, it was found that there is less particle rearrangement as the plastic deformation is less compared to the missing particle SEPUC due to a higher oleic acid overlap volume. Consequently, there is a reduced

Table 3
Young's modulus (E), Poisson's ratio (ν), shear modulus (G) and Zener ratio (a_r) of different SEPUCs obtained by uni-axial tension and pure shear simulation on elastic SCMs of respective SEPUCs.

Name	Young's modulus E [GPa]	Poisson's ratio ν [–]	Shear modulus G [GPa]	Zener ratio a_r [–]
Perfect FCC microstructure	20.101	0.30	11.615	1.5
Perturbed SEPUCs	23.636 ± 0.925	0.29 ± 0.011	10.693 ± 0.457	1.18 ± 0.032
Amorphous SEPUCs	25.180 ± 1.439	0.27 ± 0.011	10.375 ± 0.312	1.0 ± 0.038
Missing particle SEPUC	19.596	0.29	11.423	1.5
Missing particle SEPUC with correction	23.416	0.30	12.830	1.43

possibility for particles to rearrange. In any case, the differences in the residual strains are minor for the missing particle simulations.

5.2.3. Anisotropic elasticity

The results of the uniaxial tension and pure shear simulations of different SEPUCs are summarized in Table 3. The Young's modulus of the perfect FCC microstructure was calculated to be 20.1 GPa, compared to the homogeneous material's Young's modulus of 20.8 GPa, as noted in Table 1. This slight difference arises because the oleic acid parameters are optimized for both tension and shear simulations simultaneously, as detailed in Section 3.2.2. The results from the inverse analysis, shown in Fig. 8a, indicate that the optimized oleic acid material parameters result in the material behaving slightly softer than the homogeneous counterpart. The Poisson's ratio for the perfect FCC microstructure was precisely 0.3, matching the homogeneous material's properties as listed in Table 1, despite the fact that the Poisson's ratio of the homogeneous material had not been used in the process of modeling the oleic acid using inverse analysis. This alignment further underscores the robustness of the oleic acid material parameter values (Table 2) obtained via inverse analysis with different SCMs.

Regarding the effects of particle size scatter, and following the behavioral patterns discussed in Section 5.2.1, the Young's modulus (E) increased with particle scatter; amorphous SEPUCs exhibited greater stiffness than perturbed SEPUCs, followed by the perfect FCC microstructure. The Poisson's ratio (ν) and shear modulus (G) both decreased slightly with an increase in particle disorder. Consequently, the Zener ratio (a_r) approached 1.0 as particle disorder increased, achieving near isotropy for amorphous SEPUCs. Notably, the perturbed SEPUCs, which more closely represent the actual nanocomposite, exhibited a Zener ratio of only 1.18 ± 0.032, indicating significantly less anisotropy compared to the perfect FCC microstructure's anisotropic factor of 1.5. This lower level of anisotropy justifies the decision to neglect cubic material symmetry when modeling the oleic acid in Section 3.2.2, as well as the homogeneous material in a previous study [17]. A visual representation of the anisotropic elasticity of different SEPUCs is shown in Fig. 14.

Finally, the effect of the missing particle exhibited a similar trend to what was observed in Sections 5.2.1 and 5.2.2, where particle distribution and deformation played key roles. The Young's modulus (E) and shear modulus (G) remain primarily dependent on the oleic acid overlap volume. Meanwhile, the Poisson's ratio (ν) and Zener ratio (a_r) do not appear to be significantly influenced by the presence of the point defect.

6. Conclusions

The investigation into the microstructural influences on the mechanical behavior of supercrystalline magnetite oleic acid nanocomposites has yielded several key insights.

Firstly, the use of Simplified Constitutive Modeling (SCM) for inverse analysis has significantly reduced the computational costs and improved the uniqueness of the solution, albeit with the assumption of a perfect FCC microstructure. The inverse analysis performed using the 1PRF model has provided realistic material parameters for the oleic acid, highlighting significant time-dependent behavior. The results indicate that the oleic acid plays a critical role in the overall mechanical behavior of the nanocomposites, particularly under long-term loading conditions.

Secondly, the adoption of SEPUCs for realistic modeling provided a robust platform for capturing the essential features of particle size variations and defects within a manageable computational framework. The analyses demonstrate that, in general, particle size scatter improves the mechanical properties of the material. A uniform random distribution of differently sized particles across a SEPUC can lead to higher stiffness, higher creep resistance, and lower plastic deformation than a perfect FCC microstructure. This study revealed that this was due to the increase in uniformly distributed oleic acid overlap volume, leading to a higher possibility of cross-linking of oleic acid aliphatic chains during heat treatment. The presence of superlattice vacancies, considered as point defects, was shown to have a nuanced effect on the mechanical behavior. While intuitively expected to weaken the material, the results indicate that mechanical integrity is not significantly compromised. Additionally, it was found that particle scatter significantly reduces the anisotropy of the otherwise cubically symmetric perfect FCC microstructure.

Finally, the study outlines future avenues for experimental research, namely the self-assembly of oleic acid nanocomposites. Future investigations should prioritize enhancing the overlap volume of the oleic acid, which could be achieved by reducing the nearest neighbor distance (NND) or by changing the particle geometry to ellipsoidal or cuboidal shapes or by stimulating ligand extension and thus interdigitation during self-assembly. However, efforts aimed at refining the nanoparticle synthesis and the self-assembly process to minimize particle scatter or vacancies (within the specific context of isolated vacancy defects investigated here) are unlikely to enhance the mechanical properties of the materials. This suggests that future experimental efforts should focus on optimizing particle interactions (cross-linking) rather than merely striving for uniform particle distribution.

In summary, this study successfully integrates advanced computational models with realistic microstructural representation to evaluate the impact of particle size distribution and point defects in oleic acid nanocomposites. The incorporation of particle size distribution and point defects in the modeling of supercrystalline nanocomposites not only provides a more realistic assessment of their mechanical properties but also uncovers potential benefits that could be harnessed in the design of advanced materials.

Future works intend to extend this approach to explore other types of imperfections, such as stacking faults, dislocations, and cracks, and their effects, to provide a more comprehensive understanding of the mechanical behavior and failure mechanisms of these materials. Methods like the Discrete Element Method are particularly valuable for

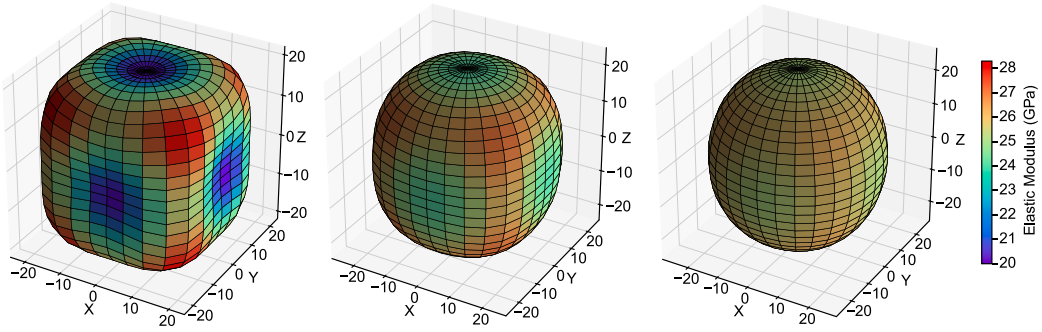

Fig. 14. Elastic modulus as a function of direction in 3D space for: (a) perfect FCC microstructure with $a_r = 1.5$ (b) perturbed SEPUCs with $a_r = 1.18 \pm 0.032$ (c) amorphous SEPUCs with $a_r = 1.0 \pm 0.038$. The color bar represents directional elastic modulus values in GPa.

incorporating these additional defect types, paving the way for the development of nanocomposites with tailored mechanical properties and more robust performance predictions across different scales and defect scenarios.

CRediT authorship contribution statement

V. Kolli: Writing – original draft, Visualization, Validation, Software, Methodology, Investigation, Formal analysis, Data curation, Conceptualization. **I. Scheider:** Writing – review & editing, Supervision, Funding acquisition. **K. Schneider:** Writing – review & editing, Methodology, Conceptualization. **D. Giuntini:** Writing – review & editing, Resources, Investigation. **C. Cyron:** Writing – review & editing, Project administration.

Declaration of competing interest

The authors declare that they have no known competing financial interests or personal relationships that could have appeared to influence the work reported in this paper.

Acknowledgments

This work was funded by the Deutsche Forschungsgemeinschaft (DFG, German Research Foundation) – SFB 986 – Project number 192 346 071. DG gratefully acknowledges the support of the Deutsche Forschungsgemeinschaft (DFG, German Research Foundation), project number GI 1471/1-1. VK thanks Yan, C. and Domènech, B. for the SEM images of the microstructure.

Data availability

Data will be made available on request.

References

[1] S. Dhulipala, D.W. Yee, Z. Zhou, R. Sun, J.E. Andrade, R.J. Macfarlane, C.M. Portela, Tunable mechanical response of self-assembled nanoparticle superlattices, Nano Lett. 23 (11) (2023) 5155–5163, http://dx.doi.org/10.1021/acs.nanolett.3c01058.

[2] P.J. Santos, P.A. Gabrys, L.Z. Zornberg, M.S. Lee, R.J. Macfarlane, Macroscopic materials assembled from nanoparticle superlattices, Nature 591 (7851) (2021) 586–591, http://dx.doi.org/10.1038/s41586-021-03355-z.

[3] E. Tam, P. Podsiadlo, E. Shevchenko, D.F. Ogletree, M.-P. Delplancke-Ogletree, P.D. Ashby, Mechanical properties of face-centered cubic supercrystals of nanocrystals, Nano Lett. 10 (7) (2010) 2363–2367, http://dx.doi.org/10.1021/nl1001313.

[4] P. Podsiadlo, G. Krylova, B. Lee, K. Critchley, D.J. Gosztola, D.V. Talapin, P.D. Ashby, E.V. Shevchenko, The role of order, nanocrystal size, and capping ligands in the collective mechanical response of three-dimensional nanocrystal solids, J. Am. Chem. Soc. 132 (26) (2010) 8953–8960, http://dx.doi.org/10.1021/ja100464a.

[5] P. Podsiadlo, B. Lee, V.B. Prakapenka, G.V. Krylova, R.D. Schaller, A. Demortiere, E.V. Shevchenko, High-pressure structural stability and elasticity of supercrystals self-assembled from nanocrystals, Nano Lett. 11 (2) (2011) 579–588, http://dx.doi.org/10.1021/nl103587u.

[6] M. Gauvin, N. Yang, Z. Yang, I. Arfaoui, M.-P. Pileni, Hierarchical mechanical behavior of cobalt supracrystals related to nanocrystallinity, Nano Res. 8 (11) (2015) 3480–3487, http://dx.doi.org/10.1007/s12274-015-0846-3.

[7] J. Wang, J. Schwenger, A. Ströbel, P. Feldner, P. Herre, S. Romeis, W. Peukert, B. Merle, N. Vogel, Mechanics of colloidal supraparticles under compression, Sci. Adv. 7 (42) (2021) eabj0954, http://dx.doi.org/10.1126/sciadv.abj0954.

[8] M.S. Lee, D.W. Yee, M. Ye, R.J. Macfarlane, Nanoparticle assembly as a materials development tool, J. Am. Chem. Soc. 144 (8) (2022) 3330–3346, http://dx.doi.org/10.1021/jacs.1c12335.

[9] D. Giuntini, S. Zhao, T. Krekeler, M. Li, M. Blankenburg, B. Bor, G. Schaan, B. Domenech, M. Müller, I. Scheider, M. Ritter, G.A. Schneider, Defects and plasticity in ultrastrong supercrystalline nanocomposites, Sci. Adv. 7 (2021) http://dx.doi.org/10.1126/sciadv.abb6063.

[10] B. Domènech, A.T.L. Tan, H. Jelitto, E. Zegarra Berodt, M. Blankenburg, O. Focke, J. Cann, C. Cem Tasan, L. Colombi Ciacchi, M. Müller, K.P. Furlan, A. John Hart, G.A. Schneider, Strong macroscale supercrystalline structures by 3D printing combined with self-assembly of ceramic functionalized nanoparticles, Adv. Eng. Mater. 22 (7) (2020) http://dx.doi.org/10.1002/adem.202000352.

[11] M.A. Boles, M. Engel, D.V. Talapin, Self-assembly of colloidal nanocrystals: From intricate structures to functional materials, Chem. Rev. 116 (18) (2016) 11220–11289, http://dx.doi.org/10.1021/acs.chemrev.6b00196.

[12] A. Dreyer, A. Feld, A. Kornowski, E.D. Yilmaz, H. Noei, A. Meyer, T. Krekeler, C. Jiao, A. Stierle, V. Abetz, H. Weller, G.A. Schneider, Organically linked iron oxide nanoparticle supercrystals with exceptional isotropic mechanical properties, Nat. Mater. 15 (2016) 522, http://dx.doi.org/10.1038/nmat4553.

[13] P. Georgopanos, G.A. Schneider, A. Dreyer, U.A. Handge, V. Filiz, A. Feld, E.D. Yilmaz, T. Krekeler, M. Ritter, H. Weller, V. Abetz, Exceptionally strong, stiff and hard hybrid material based on an elastomer and isotropically shaped ceramic nanoparticles, Sci. Rep. 7 (2017) http://dx.doi.org/10.1038/s41598-017-07521-0.

[14] B. Bor, D. Giuntini, B. Domènech, M.V. Swain, G.A. Schneider, Nanoindentation-based study of the mechanical behavior of bulk supercrystalline ceramic-organic nanocomposites, J. Eur. Ceram. Soc. 39 (10) (2019) 3247–3256, http://dx.doi.org/10.1016/j.jeurceramsoc.2019.03.053.

[15] D. Giuntini, E. Torresani, K.T. Chan, M. Blankenburg, L. Saviot, B. Bor, B. Domènech, M. Shachar, M. Müller, E.A. Olevsky, J.E. Garay, G.A. Schneider, Iron oxide-based nanostructured ceramics with tailored magnetic and mechanical properties: development of mechanically robust, bulk superparamagnetic materials, Nanoscale Adv. 1 (2019) 3139–3150, http://dx.doi.org/10.1039/C9NA00222G.

[16] A. Plunkett, M. Kampferbeck, B. Bor, U. Sazama, T. Krekeler, L. Bekaert, H. Noei, D. Giuntini, M. Fröba, A. Stierle, H. Weller, T. Vossmeyer, G.A. Schneider, B. Domènech, Strengthening engineered nanocrystal three-dimensional superlattices via ligand conformation and reactivity, ACS Nano 16 (8) (2022) 11692–11707, http://dx.doi.org/10.1021/acsnano.2c01332.

[17] V. Kolli, I. Scheider, H. Ovri, D. Giuntini, C.J. Cyron, Modeling of time-dependent mechanical behavior of oleic acid nanocomposites using nanoindentation, Mater. Today Commun. (2024) http://dx.doi.org/10.1016/j.mtcomm.2024.108892.

[18] M. Li, I. Scheider, B. Bor, B. Domènech, G.A. Schneider, D. Giuntini, Ultra-thin and ultra-strong organic interphase in nanocomposites with supercrystalline particle arrangement: Mechanical behavior identification via multiscale numerical modeling, Compos. Sci. Technol. 198 (2020) 108283, http://dx.doi.org/10.1016/j.compscitech.2020.108283.

[19] S. Ma, I. Scheider, S. Bargmann, Ultrastrong nanocomposites with interphases: Nonlocal deformation and damage behavior, Eur. J. Mech. A Solids 75 (2019) 93–108, http://dx.doi.org/10.1016/j.euromechsol.2019.01.011.

[20] B. Bor, D. Giuntini, B. Domènech, A. Plunkett, M. Kampferbeck, T. Vossmeyer, H. Weller, I. Scheider, G.A. Schneider, Constitutive and fracture behavior of ultra-strong supercrystalline nanocomposites, Appl. Phys. Rev. 8 (3) (2021-09) 031414, http://dx.doi.org/10.1063/5.0056616.
[21] P.A. Cundall, O.D.L. Strack, A discrete numerical model for granular assemblies, Géotechnique 29 (1) (1979) 47–65, http://dx.doi.org/10.1680/geot.1979.29.1.47.
[22] M. Weber, A. Spettl, M. Dosta, S. Heinrich, V. Schmidt, Simulation-based investigation of core-shell agglomerates: Influence of spatial heterogeneity in particle sizes on breakage characteristics, Comput. Mater. Sci. 137 (2017) 100–106, http://dx.doi.org/10.1016/j.commatsci.2017.05.014.
[23] J.A. Hurtado, I. Lapczyk, S.M. Govindarajan, Parallel rheological framework to model non-linear viscoelasticity, permanent set, and Mullins effect in elastomers, in: Constitutive Models for Rubber VIII, CRC Press, Boca Raton, FL, USA, 2013, pp. 113–118, http://dx.doi.org/10.1201/b14964-23.
[24] D.S. Simulia, Abaqus User's Guide.
[25] Coreform, Cubit User's Guide.
[26] K. Hitti, P. Laure, T. Coupez, L. Silva, M. Bernacki, Precise generation of complex statistical representative volume elements (RVEs) in a finite element context, Comput. Mater. Sci. 61 (2012) 224–238, http://dx.doi.org/10.1016/j.commatsci.2012.04.011.
[27] D. Balzani, L. Scheunemann, D. Brands, J. Schröder, Construction of two- and three-dimensional statistically similar RVEs for coupled micro-macro simulations, Comput. Mech. 54 (5) (2014) 1269–1284, http://dx.doi.org/10.1007/s00466-014-1057-6.
[28] D. Tal, J. Fish, Generating a statistically equivalent representative volume element with discrete defects, Compos. Struct. 153 (2016) 791–803, http://dx.doi.org/10.1016/j.compstruct.2016.06.077.
[29] K. Schneider, B. Klusemann, S. Bargmann, Fully periodic RVEs for technological relevant composites: not worth the effort!, J. Mech. Mater. Struct. 12 (4) (2017) 471–484, http://dx.doi.org/10.2140/jomms.2017.12.471.
[30] B.D. Lubachevsky, F.H. Stillinger, Geometric properties of random disk packings, J. Stat. Phys. 60 (5–6) (1990) 561–583, http://dx.doi.org/10.1007/bf01025983.
[31] B.D. Lubachevsky, How to simulate billiards and similar systems, J. Comput. Phys. 94 (2) (1991) 255–283, http://dx.doi.org/10.1016/0021-9991(91)90222-7.
[32] S. Bargmann, B. Klusemann, J. Markmann, J.E. Schnabel, K. Schneider, C. Soyarslan, J. Wilmers, Generation of 3D representative volume elements for heterogeneous materials: A review, Prog. Mater. Sci. 96 (2018) 322–384, http://dx.doi.org/10.1016/j.pmatsci.2018.02.003.
[33] S. Torquato, Random Heterogeneous Materials, Springer, 2002, http://dx.doi.org/10.1007/978-1-4757-6355-3.
[34] I. Anastasopoulos, F. Gelagoti, R. Kourkoulis, G. Gazetas, Simplified constitutive model for simulation of cyclic response of shallow foundations: Validation against laboratory tests, J. Geotech. Geoenviron. Eng. 137 (12) (2011) 1154–1168, http://dx.doi.org/10.1061/(ASCE)GT.1943-5606.0000534.
[35] Y. Li, S.-S. Guo, Y. He, Z. Liu, A simplified constitutive model for predicting shape memory polymers deformation behavior, Int. J. Comput. Mater. Sci. Eng. 04 (01) (2015) 1550001, http://dx.doi.org/10.1142/s2047684115500013.
[36] B. Isojeh, M. El-Zeghayar, F.J. Vecchio, Simplified constitutive model for fatigue behavior of concrete in compression, J. Mater. Civ. Eng. 29 (7) (2017) http://dx.doi.org/10.1061/(asce)mt.1943-5533.0001863.
[37] D. Li, C. Xiong, T. Huang, R. Wei, N. Han, F. Xing, A simplified constitutive model for corroded steel bars, Constr. Build. Mater. 186 (2018) 11–19, http://dx.doi.org/10.1016/j.conbuildmat.2018.07.019.
[38] C. Yan, B. Bor, A. Plunkett, B. Domènech, V. Maier-Kiener, D. Giuntini, Nanoindentation creep of supercrystalline nanocomposites, Mater. Des. (2022) http://dx.doi.org/10.48550/arXiv.2212.10334.